RSC Advances

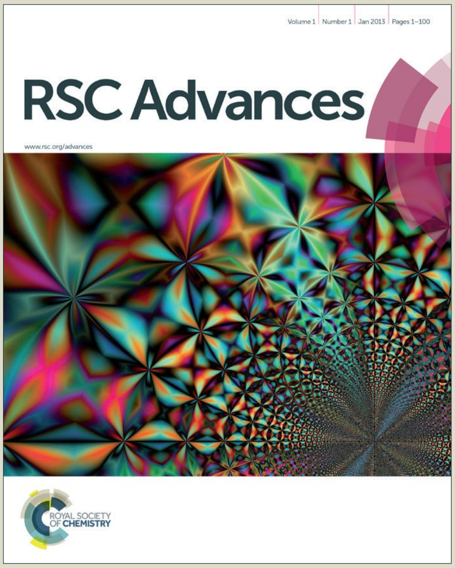

ROYAL SOCIETY OF CHEMISTRY

www.rsc.org/advances

Morphologically controllable synthesis of core-shell structured Au@Cu_2O with enhanced photocatalytic activity

Guotao Yuan[a], Mengna Lu[a], Jiuhui Fei[a], Jun Guo[a], Zuoshan Wang[a]*

Abstract: Core-shell structured Au@Cu_2O nanocomposites with different morphologies were prepared by a facile solution route. X-ray diffraction (XRD) and transmission electron microscopy (TEM) results indicated that the obtained nanocomposite consisted of gold nanorod (NR) core and Cu_2O shell, and both of them were in good crystallization. It was interested that the morphologies of the products could be tuned from octahedral to corner-truncated octahedral by changing the reductant. The results indicated that the reductant played a crucial role in determining the morphologies of as-prepared products. In addition, we investigated the photocatalytic properties of the products. It was found that both the core-shell structure and morphology of Au@Cu_2O nanocomposites had great influence on the photodegradation of MO. As a result, the Au@Cu_2O corner-truncated octahedral nanocomposites exhibited the best photocatalytic property. Our experimental results helped clarify the enhanced role of Au core and shape-dependent effect of Cu_2O NPs, which contributed to pursue more efficient photocatalysts and other promising applications.

---

* Corresponding author: No.199, Ren'ai Road, Suzhou Industry Park, Suzhou 215123, China. Tel.: +086-0512-85187680; fax: +086-0512-85187680 (Z. S. Wang). E-mail address: zuoshanwang@suda.edu.cn.

[a] College of Chemistry, Chemical Engineering and Materials Science, Soochow University, Soochow, 215123,China

1. Introduction

The fabrication of uniform heterostructure nanoparticles (NPs) with enhanced photochemical and other potential properties has received enormous research interest in catalysts, sensors, electric devices and so forth [1-3]. In this regard, noble metal NPs and semiconductor oxides have been used widely in designing multifunctional hetero systems for photocatalysis, including hydrogen production and moving of water pollution [4-6]. It is well known that the heterostructure systems have two outstanding traits: the Schottky Barrier and localized surface plasmonic resonance (LSPR), which contribute to the strong absorption of visible light and rapid charge separation. From this point, metal@semiconductor core-shell nanostructures have been a vital component in photocatalytic processes [7, 10-13].

As a typical p-type semiconductor, Cu_2O has a suitable band gap (2.17eV) and the feature of low cost, which is highly suited to be applied in photocatalysis [8, 9]. However, the rapid recombination of electron-hole pairs and the nature of growing larger in size have hindered its further applications. To improve its photocatalytic performance, large amounts of heterostructure that consist of noble metals and Cu_2O have been explored [10-14]. For instance, Wang et al have fabricated noble metal/Cu_2O heterostructure with enhanced photocatalytic performance by depositing Ag or Au nanoparticles onto Cu_2O surfaces [14]. However, noble metals NPs on the surfaces can be corrode in the process of photocatalysis, which will decrease the stability and activity of catalysts. Moreover, to utilize localized surface plasmon resonance effects, Song et al have successfully Au@Cu_2O core-shell NPs and provide a probing strategy for defect states [15]. However, it is well known that Cu_2O has shape-dependent photocatalytic properties [16, 17]. Many reports regarding Au@Cu_2O nanocomposites only focus on simple core-shell structure and ignore the shape-dependent effect [15, 18]. Therefore, further work combined the enhanced effect of noble metal with shape-dependent effect of Cu_2O in the photocatalytic area is necessary. In addition, the control of shape involved in Cu_2O is mainly via adjusting pH of the solution or the amount of reductant [19, 20]. Thus, it will also be interested to explore the role of different reductants on the morphology of Au@Cu_2O core-shell nanocomposites, and further seek for their shape-dependent effect.

In this work, we prepared two different morphologies of Au@Cu_2O core-shell NPs through a facile method, and their photocatalytic properties were evaluated by degrading MO under the excitation of visible light. In addition, the effect of core-shell structure and the morphology of the nanocomposites on the photocatalytic performance were also analyzed in details.

2. Experimental methods

In our experiments, the chemicals were of analytical grade obtained from Sinopharm Chemicals and used as received.

2.1 Synthesis of gold NRs

Gold NRs were obtained by employing a typical seed growth process [21]. To prepare the seed solution, 5 mL of $HAuCl_4$ (0.5 mM) and 5 mL of CTAB (0.2 M) solution were mixed in a bottle, and then 0.6 mL fresh $NaBH_4$ (0.01 M) was rapidly added into the mixture under vigorous stirring for 1 min. The seed solution was aged for at least 1h before use. In the process of the growth solution, 7.0 g of CTAB and 1.234 g of sodium oleate (NaOL) were dissolved in 250 mL of deionized water. The solution was kept to 30 °C. Then, 250 mL of $HAuCl_4$ (1 mM) and 24 ml $AgNO_3$ (4 mM) solution was injected. When the solution became colorless under continuous stirring, 2.1 ml of HCl solution was introduced. And then 1.25 mL of 0.064 M ascorbic acid (AA) was added under vigorously stirring for 1 min. Finally, 0.8ml of seed solution was added, and the solution was stirred for 1 min and left undisturbed at 30 °C for 12 h. The NRs were separated by centrifugation at 7500 rpm for 30 min. The obtained gold NRs was diluted into 50 ml of water.

2.2 Synthesis of Au@Cu_2O corner-truncated octahedral and bare Cu_2O

To prepare Au@Cu_2O corner-truncated octahedral, 90 mL of deionized water, 3 mL of $CuCl_2$ (0.1 M) solution, 1.01 g of sodium dodecylsulfate (SDS), 2 mL of the Au NRs solution, and 3 mL of NaOH (1 M) were introduced into a glass vial in the listed order. At last, 5 mL of H_2O solution containing 0.07 g of hydroxylamine hydrochloride was injected into the solution under vigorous stirring. After aged for 2 h at room temperature, the solution was centrifuged at 3000 rpm for 3 min. The precipitation was washed with deionized water and ethanol three times, and the washed products were dried in vacuum oven at 50 °C for 6 h. The pure Cu_2O was obtained without adding Au NRs.

2.3 Synthesis of Au@Cu_2O octahedral

Octahedral Au@Cu_2O nanocomposites were prepared through the same process as section 2.2 except that the reductant is changed to 0.3 ml of hydrazine hydrate diluted with 5 ml H_2O.

2.4 Characterization of the samples

X-ray diffraction (XRD) was employed to identify the crystalline phase of as-prepared products using Cu-Kα radiation. Scanning electron microscopy (SEM) was performed on a S4800 SEM instrument. Transmission electron microscopy and High-resolution transmission electron microscopy (TEM and HRTEM, Hitachi H600A, Tokyo, Japan.) were carried out for the morphology characterization. The UV–vis diffuse reflectance spectra of the samples were characterized by employing a UV-3600 UV–vis-NIR spectrophotometer. The specific surface areas of samples were estimated from nitrogen adsorption-desorption isotherms on a Micromeritics Tristar 3020 system.

2.5 Photocatalytic activity

The photocatalytic performance of as-prepared products was evaluated by methyl orange (MO) degradation carried out in the 100mL reactor. 500W xenon lamp as the visible light source was placed inside the reactor. A cut filter was placed between the light source and reactor, to get rid of the ultraviolet light. In typical preparation, 0.01g of the samples was dispersed into 100 mL of MO solution (10 mg/L). The mixture was kept in the dark for 20 min before irradiation. After irradiation, the mixture was taken out every 20 min. The products were analyzed by employing the UV-vis spectrophotometer. Through the formula $\eta=C/C_o$, where C_0 represented for the concentration of the original MO solution and C represented for the concentration of MO solution taken out every 20 min, the residual proportion of MO could be figured out. Therefore, the degradation curves and rates of MO solution were obtained.

3. Results and discussion

The crystal structures of the as-prepared samples were characterized by XRD. **Fig. 1** was typical XRD patterns of products. The XRD patterns of Au@Cu_2O contained two sets of diffraction data, in which the peaks at 29.6°, 36.5°, 42.4°, 61.5°, and 73.6° corresponded to the characteristic peaks of the cubic phase Cu_2O (JCPDS No.05-0667) and the other peaks at 38.2°, 44.4°, 64.7° and 77.5° could be assigned to the cubic Au (JCPDS No.89-3697), respectively. The XRD results suggested the formation of Au and Cu_2O crystals. No peaks corresponding to impurities like CuO were observed.

In order to further investigate the morphology of samples, TEM test was carried out. The TEM image of Au NRs showed the monodisperse Au NRs with a length and width of around 100 nm and 16 nm, respectively (**Fig. 2a**). HRTEM image of **Fig. 2b** displayed the lattice fringes of 2.36 Å, corresponding to (111) facets of Au NRs. From **Fig. 2c**, it could be clearly seen that Au NRs located in the central area. Cu and Au element distributions from the line scanning (**Fig. 2d**) agreed well with the microscopic image.

The SEM image (**Fig. 3a**) showed that the Au@Cu_2O photocatalyst had the corner-truncated octahedral shell (OCT-Au@Cu_2O), and also gave an average size of *ca.* 110nm. It was clear from the TEM image of **Fig. 3b** that all core-shell NPs encompassed only one Au NR and barely particles with excess cores or no core were found, which manifested the successful coating of Cu_2O over Au NRs. The HRTEM image of **Fig. 3c** in the selected area (white marked region) illuminated the interplanar spacing of 2.45 Å, assigned to the spacing of the (111) plane of Cu_2O, which closed to interplanar spacing of Au (111) (2.36 Å). This result demonstrated the epitaxial formation of Cu_2O shell in the interface. However, the HRTEM image in **Fig. 3d** showed the [110] growth direction, indicating that the exposed faces of core-shell NPs were {110} facets.

When $N_2H_4 \cdot H_2O$ was employed as a reductant, Au@Cu_2O NPs displayed the information of octahedral shell (O-Au@Cu_2O). The TEM image of **Fig. 4b** exhibited that the core-shell NPs were an average size of *ca.* 106nm. The HRTEM image in **Fig. 4c** revealed the interplannar spacing of 3.0 Å, corresponding to (110) plane of cubic Cu_2O, which had a big lattice mismatch by comparing the lattice fringes with Au NRs. This result indicated $N_2H_4 \cdot H_2O$ had a special impact on the information of the heterostructure (as showed in scheme 1). **Fig. 4d** showed the [111] growth direction, indicating that the exposed facets of core-shell NPs were {111} facets.

By change the reductant, the morphology of Au@Cu_2O was tuned from octahedral to corner-truncated octahedral. A possible mechanism was proposed as showed in **Scheme 1**. In the role of SDS, $Cu(OH)_4^{2-}$ species were attracted around Au NRs. Once the reductant was added into the reaction, Cu^{2+} was immediately reduced to Cu^+. Differently, N_2H_4 as a pair of hands connected $Cu(OH)_4^{2-}$ species with Au NRs, which contributed to the hetero growth of Cu_2O. At the same time, N_2H_4 as a strong reductant facilitated the octahedron shell of Cu_2O, which was its most stable morphology [22]. Thus, O-Au@Cu_2O exposed the {111} facets. However, $N_2OH \bullet HCl$ might be regarded as a surfactant to adsorb on the {110} facets of Cu_2O and prevent the growth of {110} facets. Thus, OCT-Au@Cu_2O exposed the {110} facets.

As a contrast, bare Cu_2O NPs were obtained without adding Au core in the reaction medium. The SEM and TEM images (**Fig. 5)** testified the octahedral structure of Cu_2O NPs with the size of around 460 nm. The difference of size between bare Cu_2O and Au@Cu_2O NPs indicated that Au cores had an outstanding impact on the size of Cu_2O shell, which contributed to construct small size, high specific surface area, and monodisperse NPs. The SAED pattern exhibited uniform and regular bright pots (showed in **Fig. 5c**), which indicated the single crystalline nature of the cubic phase Cu_2O and the growth along the [110] direction. The HRTEM image showed the lattice fringes at 3.0 Å, which was corresponding to the (110) facets of Cu_2O (**Fig. 5d**).

As described above, we prepared two different types of Au@Cu_2O core-shell structures by employing two different reductants. The UV-vis diffuse reflectance spectra test was carried out to investigate the optics effect of as-prepared samples. As observed in **Fig. 6**, Au@Cu_2O nanocomposites showed a wide range of absorption in visible-light area, which indicated the visible-light-driven photocatalytic ability. The photodegradation of MO solution was performed to investigate their photocatalytic properties. **Fig. 7** displayed the photocatalytic degradation of MO solution under visible irradiation using as-prepared samples as the photocatalysts. It was observed that about 94% of MO had been degraded using OCT-Au@Cu_2O as a photocatalyst for 80min under irradiation of 500 W xenon lamp, which was better than that of other samples.

To further demonstrate the role of Au core, the electron-transfer process of Au@Cu_2O structure on photogradation of MO was pictorially presented, as showed in **Scheme 2**. It was believed that the photo-excited electron in the conduction band of Cu_2O could transfer to Au NRs due to the Schottky barrier at the metal-semiconductor interface, which could be considered as direct electron transfer (DET). However, due to the effect of plasmon-induced resonant energy transfer (PIRET), the photo-excited electrons could facilitate separation of electron-hole pairs in semiconductor [23, 24]. Thus, the electron-transfer process of Au@Cu_2O could be summed up as the synergistic effect of DET and PIRET.

In view of a higher ratio of adsorption showed in **Fig. 7**, we believed that OCT-Au@Cu_2O exposing {110} planes were more selective for adsorption of MO compared with O-Au@Cu_2O exposing {111} planes, which indicated the enhanced photocatalytic ability of OCT-Au@Cu_2O. This result was in agreement with a previous report [25]. In addition, due to the different surface energy and the density of copper dangling bonds of {111} and {110} facets, the synergistic effect can facilitate the spatial charge separation and thus improve the photocatalytic activity [26, 27].

However, the exploration on this topic needs us further work.

In order to estimate the effect of specific surface areas of Au@Cu_2O nanocomposites, nitrogen adsorption-desorption isotherms from the BET test were analyzed. The nitrogen adsorption-desorption isotherms were of type IV. As shown in **Fig. 8**, the specific surface areas of OCT-Au@Cu_2O and O-Au@Cu_2O were 12.6 m^2/g and 10.8 m^2/g, respectively. This result revealed that Au@Cu_2O nanocomposites had similar specific surface areas.

Thus, the enhanced photocatalytic property of the Au@Cu_2O core-shell NPs could be ascribed to the role of Au core and shape-dependent photocatalytic properties of Cu_2O shell. These results indicated that the shape and size control of Au@Cu_2O core-shell structure NPs could be greatly helpful to improve the photocatalytic activity of the catalysts.

3. Conclusion

In summary, we have developed a facile strategy to obtain two morphologies of Au@Cu_2O core-shell NPs for the photocatalytic degradation of MO. The morphology of core-shell structures was tuned from octahedral to corner-truncated octahedral by changing the reductant. Au@Cu_2O corner-truncated octahedral NPs were found to display more enhanced photocatalytic performance, which could be ascribed to the role of Au NRs and shape-dependent photocatalytic properties of Cu_2O NPs. We therefore demonstrate obviously enhanced effect of morphologically controlled core-shell NPs on photocatalysis, which contributes to explore more promising applications, such as sensor and solar cell, not only in the respect of photocatalysis.

Acknowledgements

The authors are grateful for the financial support of a project funded by the Priority Academic Program Development of Jiangsu Higher Education Institutions and a key project for Industry-Academia-Research in Jiangsu province (BY2013030-04). This study is also supported by Testing and Analysis Center Soochow University.

Reference

1 H. Wang, L. Zhang, Z. Chen, J. Hu, S. Li, Z. Wang, J. Liu and X. Wang, *Chem. Soc. Rev.*, 2014, **43**, 5234.
2 K. T. Nguyen and Y. Zhao, *Nanoscale*, 2014, **6**, 6245.
3 Q. Zhang, I. Lee, J. B. Joo, F. Zaera, and Y. Yin, *Acc. Chem. Res.,* 2013, **46**, 1816.
4 N. Zhou, L. Polavarapu, N. Gao, Y. Pan, P. Yuan, Q. Wang and Q. Xu, *Nanoscale*, 2013, **5**, 4236.
5 Y. Chen, D. Zeng, K. Zhang, A. Lu, L. Wanga and D. Peng, *Nanoscale.*, 2014, **6**, 874.
6 Z. Wu, Y. Xue, H. Wang, Y. Wu and H. Yu, *RSC Adv.*, 2014, **4**, 59009.
7 Y. Zhang, B. Deng, T. Zhang, D. Gao and A. Xu, *J. Phys. Chem. C*, 2010, **114**, 5073.
8 C. M. McShane and K. S. Choi, *J. Am. Chem. Soc.*, 2009, **131**,2561.
9 L. Wu, L. K. Tsui, N. Swami and G. Zangari, *J. Phys. Chem. C*, 2010, **114**, 11551.
10 J. Xiong, Z. Li, J. Chen, S. Zhang, L. Wang and S. Dou, *ACS Appl. Mater. Interfaces*., 2014, **6**, 15716.
11 L. Sinatra, A. P. LaGrow, W. Peng, A. R. Kirmani, A. Amassian, H. Idriss, O. M. Bakr, *J. Catal.*, 2015, **322**, 109.
12 L. Kong, W. Chen, D. Ma, Y. Yang, S. Liu and S. Huang, *J. Mater. Chem.*, 2012, **22**, 719.
13 S. K. Cushing, J. Li, F. Meng, T. R. Senty, S. Suri, M. Zhi, M. Li, A. D. Bristow and N. Wu, *J. Am. Chem. Soc.,* 2012, **134**, 15033.
14 Z. Wang, S. Zhao, S. Zhu, Y. Sun and M. Fang, *CrystEngComm.*, 2011, **13**, 2262.
15 X. Shi, Y. Ji, S. Hou, W. Liu, H. Zhang, T. Wen, J. Yan, M, Song, Z. Hu and X. Wu, *Langmuir*, 2015, **31**, 1537.
16 C.-H. Kuo, Y.-C. Yang, S. Gwo and M. H. Huang, *J. Am. Chem. Soc.*, 2011, **133**, 1052.
17 W.-C. Wang, L.-M. Lyu and M. H. Huang, *Chem. Mater.*, 2011, **23**, 2677.
18 S. Ren, B. Wang, H. Zhang, P. Ding and Q. Wang, *ACS Appl. Mater. Interfaces,* 2015, **7**, 4066.
19 Y. Zhang, B. Deng, T. Zhang, D. Gao, A.-W. Xu, *J. Phys. Chem. C,* 2010,**114,** 5073.
20 H. Xu, W. Wang, W. Zhu, *J. Phys. Chem. B*, 2006, **110,** 13829.
21 X. Ye, C. Zheng, J. Chen, Y. Gao and C. B. Murray, *Nano Lett.*, 2013, **13**, 765.
22 Z. Zheng, B. Huang, Z. Wang, M. Guo, X. Qin, X. Zhang, P. Wang, Y. Dai, *J. Phys. Chem. C*, 2009, **113,** 14448.
23 S. K. Cushing, J. Li, F. Meng, T. R. Senty, S. Suri, M. Zhi, M. Li, A. D. Bristow and N. Q. Wu, *J. Am. Chem. Soc.*, 2012, **134**, 15033.
24 A. Furube, L. Du, K. Hara, R. Katoh and M. Tachiya, *J. Am. Chem. Soc.*, 2007, **129**, 14852.

25 W.-C. Huang, L.-M. Lyu, Y.-C. Yang and M. H. Huang, *J. Am. Chem. Soc.*, 2012, **134**, 1261.

26 Y. Zhang, B. Deng, T. Zhang, D. Gao, A.-W. Xu, *J. Phys. Chem. C*, 2010, **114**, 5073.

27 Q. Hua, T. Cao, X.-K. Gu, J. Lu, Z. Jiang, X. Pan, L. Luo, W.-X. Li, and W. Huang, *Angew. Chem. Int. Ed.*, 2014, **53**, 4856.

Figure caption

Figure 1 XRD patterns of as-prepared samples

Figure 2 (a) TEM and (b) HRTEM images of Au NRs; (c) STEM image of Au@Cu_2O corner-truncated octahedral; (d) cross-sectional compositional line profiles of Cu and Au elements

Figure 3 (a) SEM and (b) TEM images of Au@Cu_2O corner-truncated octahedral; (c) and (d) HRTEM images of selected area.

Figure 4 (a) SEM and (b) TEM images of Au@Cu_2O octahedral; (c) and (d) HRTEM images of selected area.

Scheme 1 Illustration of the formation of Au@Cu_2O samples.

Figure 5 (a) SEM; (b) TEM images; (c) SAED pattern and HRTEM image of Cu_2O NPs.

Figure 6 UV-vis diffuse reflectance spectra of Au NRs and Au@Cu_2O samples.

Figure 7 The degradation curves of MO under visible light irradiation.

Scheme 2 Pictorial illustration of electron-transfer process of OCT-Au@Cu_2O

Figure 8 N_2 adsorption-desorption isotherms of Au@Cu_2O.

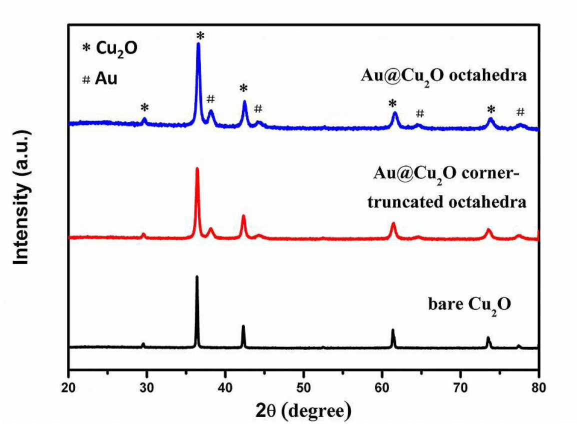
* Cu_2O
# Au
Au@Cu_2O octahedra
Au@Cu_2O corner-truncated octahedra
bare Cu_2O
Intensity (a.u.)
20
30
40
50
60
70
80
2θ (degree)

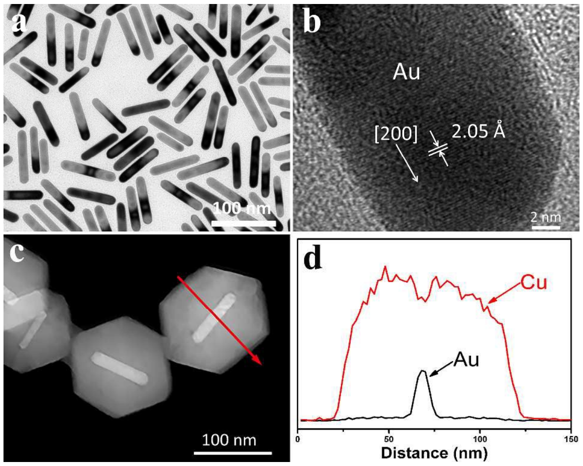
a
100 nm
b
Au
[200]
2.05 Å
2 nm
c
100 nm
d
Cu
Au
0
50
100
150
Distance (nm)

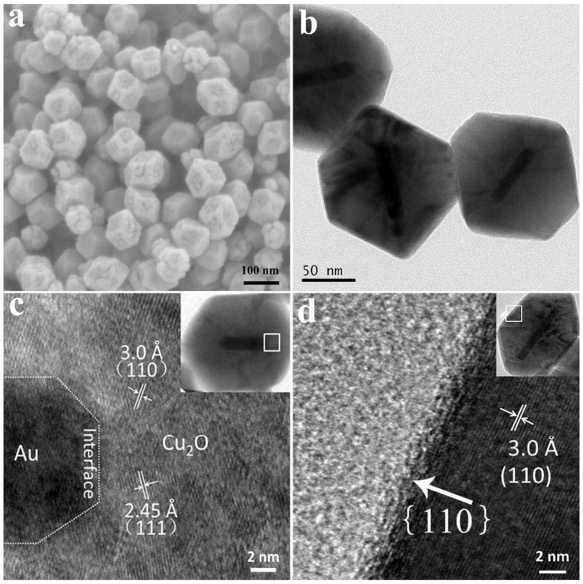
a
100 nm
b
50 nm
c
3.0 Å
(110)
Au
Interface
Cu_2O
2.45 Å
(111)
2 nm
d
3.0 Å
(110)
{110}
2 nm

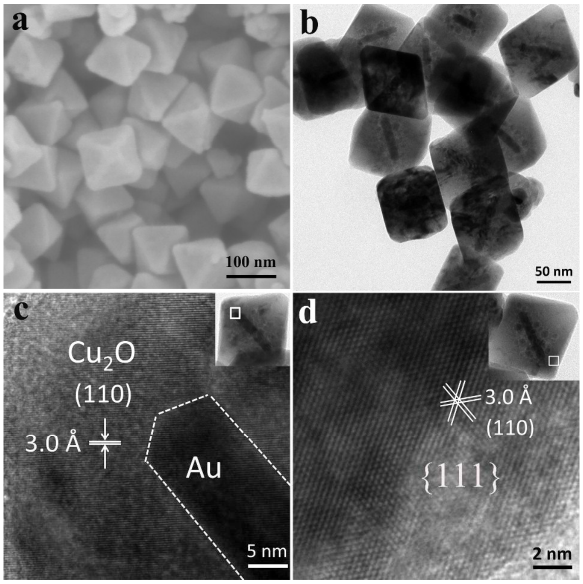
a
100 nm
b
50 nm
c
Cu$_2$O
(110)
3.0 Å
Au
5 nm
d
3.0 Å
(110)
{111}
2 nm

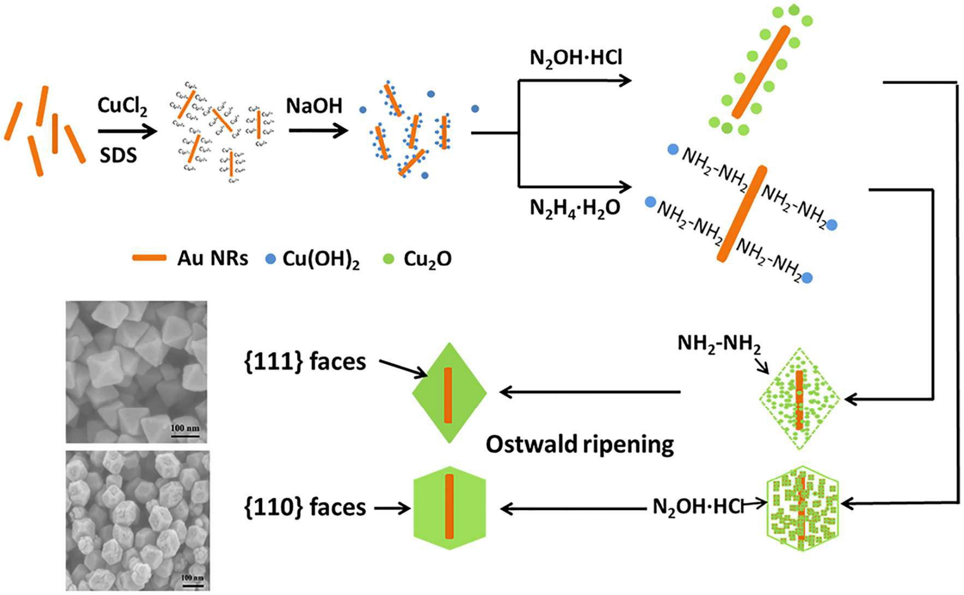
CuCl$_2$
SDS
NaOH
N$_2$OH·HCl
N$_2$H$_4$·H$_2$O
NH$_2$-NH$_2$
NH$_2$-NH$_2$
NH$_2$-NH$_2$
NH$_2$-NH$_2$
Au NRs
Cu(OH)$_2$
Cu$_2$O
{111} faces
NH$_2$-NH$_2$
Ostwald ripening
{110} faces
N$_2$OH·HCl
100 nm
100 nm

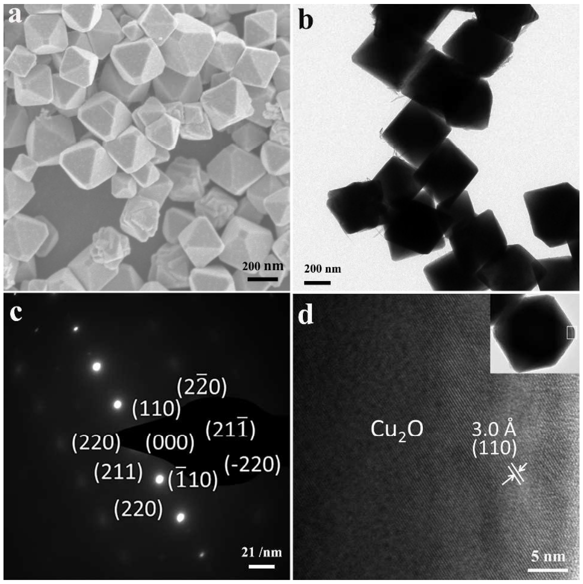
a
200 nm
b
200 nm
c
(2$\bar{2}$0)
(110)
(220)
(000)
(21$\bar{1}$)
(-220)
(211)
($\bar{1}$10)
(220)
21 /nm
d
Cu$_2$O
3.0 Å
(110)
5 nm

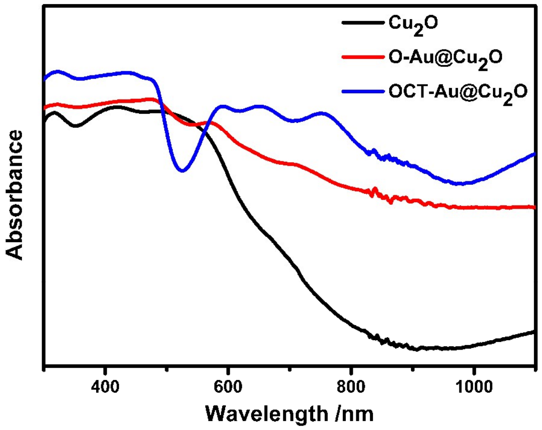
Cu$_2$O
O-Au@Cu$_2$O
OCT-Au@Cu$_2$O
Absorbance
400
600
800
1000
Wavelength /nm

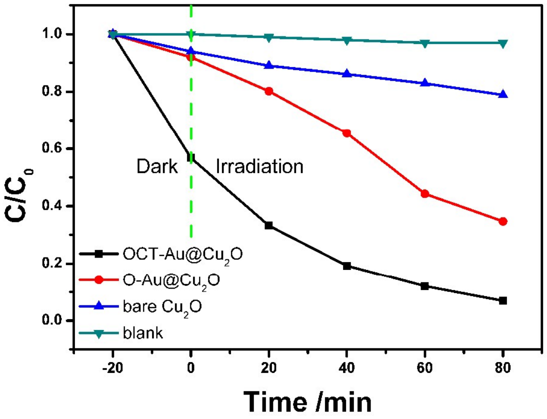
1.0
0.8
0.6
0.4
0.2
0.0
C/C$_0$
Dark
Irradiation
OCT-Au@Cu$_2$O
O-Au@Cu$_2$O
bare Cu$_2$O
blank
-20
0
20
40
60
80
Time /min

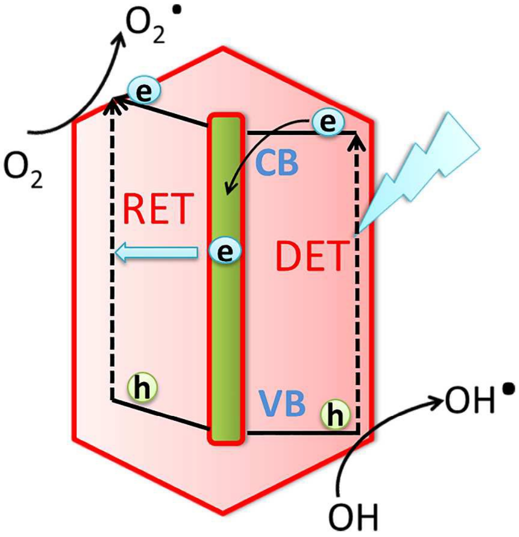
$O_2^\bullet$
e
O_2
e
CB
RET
e
DET
h
VB
h
$OH^\bullet$
OH

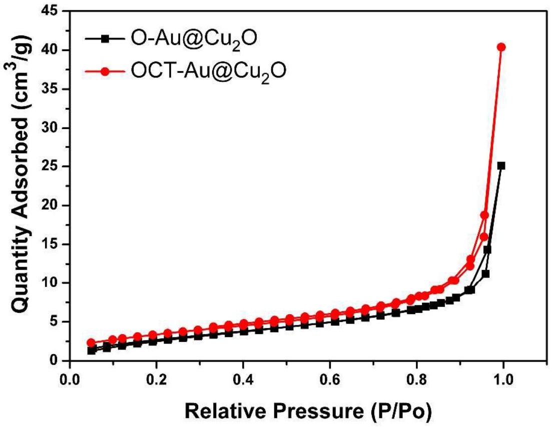
O-Au@Cu_2O
OCT-Au@Cu_2O
Quantity Adsorbed (cm^3/g)
0
5
10
15
20
25
30
35
40
45
0.0
0.2
0.4
0.6
0.8
1.0
Relative Pressure (P/Po)